Transient shear banding of highly polydisperse polymer binary and ternary solutions and concentration effects

Can-Qi Li, Yuan-Qi Fan, Zhuo Hong, Alfredo Lanzaro, Xue-Feng Yuan*

Institute for Systems Rheology, Guangzhou University, No.230 West Outer Ring Road, Higher Education Mega-Center, Panyu District, Guangzhou 510006, P. R. China.

Abstract

Universality of shear banding has been studied by rheometric characterisation and computational simulation of polydisperse and high molecular weight polyacrylamide aqueous solution. The rheological results show that the slope of the steady-state shear stress of the polymer solution in the medium shear rate range decreases with the increase of concentration, while the steady-state shear stress of 500c* is basically independent of the shear rate, which is a general feature of the existence of the shear banding. Taking the results of the steady-state flow experiment of 500c* as a reference, the two-dimensional and three-dimensional simple shear flow simulation study was calculated, and the calculation results found that when the steady-state shear stress is weakly dependent on the shear rate, the velocity field distribution within this shear rate range shows that a transient shear banding is generated, and the existence of the transient shear banding depends on the number of *Wi* applied. The larger the number of *Wi*, the longer the transient shear banding will exist.

I. INTRODUCTION

Shear banding is a common phenomenon observed firstly in worm-like micellar solutions[1] and subsequently in other complex fluids[2] including entangled polymer solutions, suspensions, liquid crystals and soft glassy materials, *etc*. A generic feature of those complex fluids under shear flow is that there is a characteristic shear rate above which the shear stress is nearly independent of the applied nominal shear rate. Studies of the shear stress plateau region by birefringence[3,4], nuclear magnetic resonances (NMR) velocity imaging[5,6], particle tracking velocimetry[7] and optical coherence tomography technique[8] have revealed the existence of the banded flow with different values of the local shear rate. The proportion of the high and low shear rate bands depends upon the nominal shear rate.

In order to account for the dynamics of wormlike micelle solutions under linear and nonlinear flow, Cates and co-workers[9,10] have extended the Doi–Edwards model[11] for entangled polymers by incorporating the reptation dynamics with the breaking-recombining process and proposed a reptation-reaction model. In the fast breaking limit, the rapid breaking-recombining reaction has a pre-average effect on the reptation time spectrum due to polydispersity of the micellar lengths and results in a well-defined characteristic relaxation time. The model resembles the Maxwell fluid behavior with a single relaxation time at low frequencies in the linear viscoelastic regime. In the nonlinear regime, the model inherits a characteristic feature of the original Doi–Edwards model, which exhibits nonmonotonic behavior under homogeneous shear flow, *i.e.*, there is a region where a given stress corresponds to multiple values of the strain rate. The shear banding was initially studied in terms of a mechanical instability due to the nonmonotonic behavior of the constitutive model under Couette and Poiseuille flows[12-16]. It was then investigated under the theoretical framework of the two-fluid model[17], which accounts for flow-induced phase transitions and the mechanical instabilities by directly coupling viscoelastic stress and diffusive fluid composition. This allows to study the interplay between thermodynamics and hydrodynamics of complex fluid flows in a unified manner[18-23]. The model can select a steady state stress in a physical way for nonmonotonic constitutive equations under strong flow and directly correlate the mechanical shear band formation to the formation of fluid composition bands. In addition to the usual thermodynamic parameters for determining equilibrium phase behavior, the degree of dynamic asymmetry, characterized by the ratio of the moduli and the ratio of the relaxation time between the two phases of the fluid, governs dynamical phase behaviour[18,19]. The larger the dynamic contrast of two components, the bigger the shift of the equilibrium phase boundary under flow conditions.

In contrast to wormlike micelle solutions, polymer solutions and melts exhibit multiple scale dynamics with a wide range of relaxation times. The relaxation spectrum could be significantly broadened by molecular mechanism such as contour-length fluctuations and constraint release. Furthermore, by incorporating convective constraint release (CCR)[24,25] with an adjustable parameter, the nonlinear behavior of the original Doi-Edwards model could be tunable, so that either nonmonotonic or monotonic behavior could be observed depending on the effectiveness of constraint release. It has been shown[26] that the shear banding could occur in complex fluid flow as long as its steady-state shear stress exhibits a small

*Institute for Systems Rheology, Guangzhou University, No.230 West Outer Ring Road, Higher Education Mega-Center, Panyu District, Guangzhou 510006, P. R. China. Corresponding author E-mail: xuefeng.yuan@gzhu.edu.cn

gradient over a range of the applied nominal shear rate. Coarse-grained molecular dynamic simulations of entangled monodisperse polymer melts[27] reproduced the typical experimental results[28,29] of transient and steady shear banding after the stress overshoot for monotonic and nonmonotonic flow curves, respectively. Dissipative Particle Dynamics simulations[30-32] further revealed that the shear banding occurs due to inhomogeneous chain segmental orientation and entanglement density of polymeric fluids. Their onset and underlying molecular mechanism are generally universal. The higher polydispersity index of polymer melts is, the larger the effect of broadening the stress plateau. For polymeric melts with sufficiently long chain, shear banding could be remained indefinitely. For shorter chain melts, transient shear banding could be observed after the appearance of a stress overshoot, but then decayed after the stresses had attained their steady state.

Over the last decades, a significant progress has been made on the better understanding of shear banding and dynamic mechanism of monodisperse flexible polymer solutions. However, the effects of polydispersity still remain elusive. In this paper, shear banding and its concentration dependence of commercially relevant polydisperse high molecular weight polyacrylamide solution will be studied by rheological characterization and computer simulations. In Section II, the experimental and computational methods will be introduced. The results and discussion are reported in Section III. The conclusions are drawn in Section IV.

II. METHODOLOGY

A. Polymer solution

A sample of commercially available polyacrylamide (PAAm) with a nominal average molecular weight (Mw) of 18×10^6 g/mol was purchased from Polysciences, Inc (Catalogue No.: 18522-100) and used as received (here after called as 18M PAAm). It was dissolved in deionized water and in 60*wt.*% sucrose-deionized-water solution, respectively, to form 18M PAAm binary and ternary solutions. The average radius of gyration can be estimated by the nominal molecular weight (M) as $R_g = 0.0749M^{0.64\pm0.01}$(Å)[33], hence R_g = 329.5nm. Due to lack of the standard high molecular weight polymer sample, quantitative characterization of molecular weight and distribution of 18M PAAm sample by Gel Permeation Chromatography is very difficult if not impossible. However, it may be reasonably expected that its polydispersity index would be significantly higher than 5M PAAm sample of Mw=5.7×10^6 g/mol and M_w/M_n = 34.4, supplied by the same source and characterized in our previous work.[34] Using a simple cubic packing assumption, the overlap concentration was estimated as c^*= 0.00946 *wt.*%. A series of 18M PAAm binary and ternary solutions were prepared and studied respectively in a semi-dilute entangled concentration range from 9.6c* (0.096*wt.*%) to 500c* (5*wt.*%) approximately.

B. Rheometry

The rheological properties of 18M PAAm binary and ternary solutions were measured at a constant temperature of 25℃ using an ARES-G2 shear rheometer (TA Instruments). A cone-plate fixture (diameter= 50 mm, angle=0.04 rad) was used. The plate was coupled with an Advanced Peltier System (APS) connected to a ThermoCube Model 10-300 (115/230 V, 50/60 Hz) water bath system with temperature control accuracy of ± 0.2℃.

C. Computational method

The motion of an incompressible, isothermal viscoelastic fluid is governed by the continuity equation,

$$\boldsymbol{\nabla}\cdot\mathbf{v}=0 \quad , \tag{1}$$

where $\mathbf{v}$ is the velocity, and the momentum balance equation,

$$\rho\left(\frac{\partial\mathbf{v}}{\partial t}+\mathbf{v}\cdot\boldsymbol{\nabla}\mathbf{v}\right)=-\boldsymbol{\nabla}p+\boldsymbol{\nabla}\cdot\boldsymbol{\tau}(t) \quad , \tag{2}$$

where ρ is the fluid density, p is the isotropic pressure, and $\boldsymbol{\tau}$ is the extra-stress tensor. The extra-stress of viscoelastic fluid consists of two parts, the first part is the contribution of solvent and the other part is the contribution of polymer, as shown below,

$$\boldsymbol{\tau}(t)=\eta_s(\nabla\mathbf{v}+\nabla\mathbf{v}^T)+\boldsymbol{\tau}_p(t) \quad , \tag{3}$$

where η_s is the viscosity of solvent, $\boldsymbol{\tau}_p(t)$ is the polymeric stress and will be defined by a constitutive model.

Doi and Edwards pioneered the molecular theory of entangled polymer dynamics based on tube model in 1978.[11] The Rolie-Poly model[35] used for modeling transient shear banding of polymer solutions in the present study is a simplified version of the full Doi and Edwards molecular theory.[36] It could account for the main dynamic mechanisms of entangled polymer chains, including reptation, convective constraint release, chain stretch etc. The conformation tensor of polymer chain $\mathbf{A}(t)$ in a velocity field $\mathbf{v}$ evolves in time as

$$\frac{D\mathbf{A}}{Dt}=\mathbf{L}\cdot\mathbf{A}+\mathbf{A}\cdot\mathbf{L}^T+f(\mathbf{A}) \tag{4}$$

where $\frac{D\mathbf{A}}{Dt}$ is the materials derivative, $\mathbf{L}=\boldsymbol{\nabla}\mathbf{v}$ is the velocity gradient tensor and $\mathbf{L}^T$ is its transpose. The model function $f(\mathbf{A})$ is defined by the non-Gaussian version of the Rolie-Poly constitutive model.[37] It could account for the finite extensibility of polymer chains and is given by

$$f(\mathbf{A}) = -\frac{1}{\lambda_D}(\boldsymbol{A}-\boldsymbol{I}) - \frac{2}{\lambda_R}k_s(\chi)\left(1-\sqrt{\frac{3}{tr(\boldsymbol{A})}}\right)\left[\boldsymbol{A}+\beta\left(\frac{tr(\boldsymbol{A})}{3}\right)^{\delta}(\boldsymbol{A}-\boldsymbol{I})\right], \quad (5)$$

where $\boldsymbol{I}$ is the unit tensor, λ_D is the reptation time or the disengagement time of entangled polymer chain, λ_R is the longest Rouse time or stretch time of polymer chain, β is the coefficient of the convective constraint release, $k_s(\chi)$ is the nonlinear spring coefficient and is approximated by

$$k_s(\lambda) = \frac{\left(3-\frac{\chi^2}{\chi_{\max}^2}\right)\left(1-\frac{1}{\chi_{\max}^2}\right)}{\left(1-\frac{\chi^2}{\chi_{\max}^2}\right)\left(3-\frac{1}{\chi_{\max}^2}\right)}, \quad (6)$$

Where $\chi = \sqrt{tr(\mathbf{A})/3}$ is the chain stretch ratio with respect to its equilibrium conformation, $\chi_{\max}$ is the fixed maximum stretch ratio of polymer chains. Thus, the polymeric stress could be readily calculated from its conformation tensor A by

$$\boldsymbol{\tau}_p(t) = Gk_s(\lambda)[\mathbf{A}(t)-\boldsymbol{I}] = \frac{\eta_p}{\lambda_D}k_s(\lambda)[\mathbf{A}(t)-\boldsymbol{I}], \quad (7)$$

where $G = \frac{\eta_p}{\lambda_D}$ is the plateau modulus and η_p is the zero-shear polymer viscosity. Further details about the Rolie-Poly model could be found elsewhere.[35,37]

The above continuity, momentum and constitutive equations are discretized using the finite volume method based on OpenFOAM CFD toolbox, released by OpenCFD Ltd, and solved by a viscoelastic fluid flow solver available in RheoTool. The terms of diffusion, gradient and divergence in the governing equations are discretized by the central differencing scheme. The convection terms are discretized by the MINMOD scheme. The temporal terms are discretized by the backward scheme. The above discretization produces a system of linear equations to relate the cell face values of the unknown eld variables at current time to their values at previous time and at the neighboring cell centers. The system can be solved by one of the iterative matrix solvers, including the conjugate (PCG) and biconjugate gradient (PBiCG) methods, available in the Open-FOAM toolbox. The details can be found in the OpenFOAM and RheoTool User Guide, respectively.[38,39]

III. RESULTS AND DISCUSSION

A. Linear viscoelasticity

18M PAAm binary and ternary solutions with various concentrations were characterised in the linear viscoelastic region under the small-amplitude oscillatory shear flow in a range of frequencies and a constant 2% strain amplitude. The results are shown in Fig.1. In analogy to the time-temperature superposition (TTS) principle, the concentration dependence of the rheometric properties of polymer solutions can be analyzed by applying the time-concentration superposition (TCS) procedure to the data presented in Fig.1. With respect to an arbitrary reference concentration (set as 500c* and 92.1c* for 18M PAAm binary and ternary solution, respectively), a master curve of storage modulus (G'), loss modulus (G") and complex viscosity (η*) could be obtained by shifting their linear viscoelastic data horizontally by a factor a_c and vertically by a factor b_c, respectively. Since the concentration scaling of Rouse dynamics is different from the terminal flow dynamics dominated by the entanglement dynamics, the TCS could only be realized either in the terminal dynamic regime or in the Rouse regime. In the present work, the TCS is applied in the terminal dynamic regime for the binary solutions and in the Rouse regime for the ternary solutions, respectively, as shown in Fig.2. Thus, the shifted storage and loss moduli of various concentrations are not so well superimposed in the high frequency region for the binary solutions and in the low frequency region for the ternary solutions.

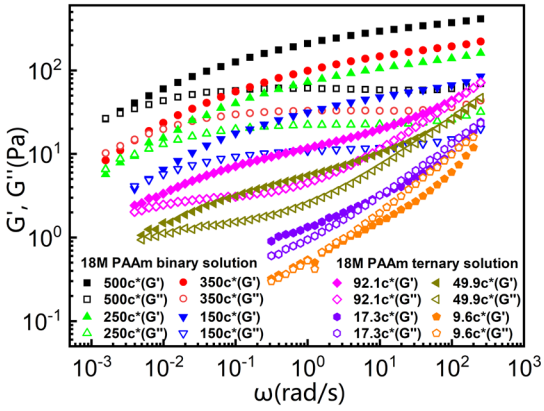

Fig.1 The storage modulus G' and the loss modulus G'' of the 18M PAAm binary and ternary solution as a function of angular frequency.

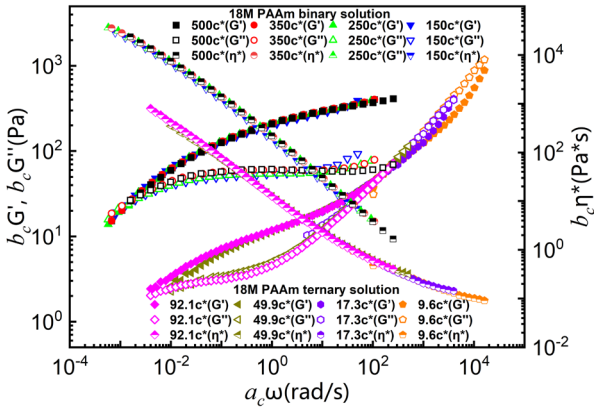

Fig.2 A master curve of storage modulus (G') and loss modulus (G"), complex viscosity after shifting the linear viscoelastic data of the semi-dilute 18M PAAm binary and ternary solutions horizontally by a factor a_c and vertically by a factor b_c, with respect to c_{ref}=500c* and c_{ref}=92.1c*, respectively.

If considering the shifting factors a_c and b_c as a reduced frequency (or equivalently an inverse of a characteristic time) and a reduced plateau modulus, respectively, the ratio of the shifting factors could be related to the complex viscosity and scaled with polymer concentration as a_c/b_c. Fig.3 plots a_c,1/ b_c,

a_c/b_c as a function of (c_{ref}/c) in the logarithmic scales.[40] The plot exhibits a well-defined power law scaling with the relevant exponent, which actually resembles the concentration scaling exponent of characteristic time, modulus and complex shear viscosity, respectively. Within the standard deviation, the same scaling exponents of the 18M PAAm binary solutions over a wide concentration range from 10c* to 500c* are found.[40] However for the ternary solutions, in which the TCS is applied in the Rouse regime, the concentration scaling exponent of the Rouse time is negative, *i.e.* -1.9±0.1, which is approximately same as the exponent of the modulus. Hence, it results in the independence of its complex viscosity with polymer concentration.

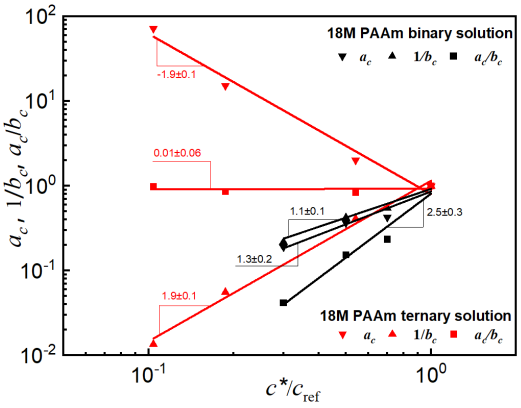

Fig.3 The concentration scaling of the shifting factor a_c, b_c and a_c/b_c to obtain the master curves of G', G" and η* in Fig.2 for the semi-dilute entangled 18M PAAm binary (c_{ref}=500c*) and ternary (c_{ref}=92.1c*) solutions.

B. Non-linear shear rheometric properties

All the samples are characterized by the steady shear experiment. In Fig.4, the steady shear stress (σ), the shear viscosity (η) and the first normal stress difference (N_1) are plotted as a function of shear rates for the 18M PAAm binary and ternary solutions in various concentrations, respectively. The TCS principle is also extended in the analysis of their concentration dependence. By choosing c_{ref}=500c* and c_{ref}=92.1c*, respectively, and using appropriate shift factors, the steady rheometric property curves could be superimposed as shown in Fig.5. The suitable horizontal shifting factors a_c for the superposition of the steady rheometric properties have little difference from those used for the construction of the master curves in Fig. 2. However, the different vertical shift factors b_c' and b_c'' are usually required due to the difference of the linear and nonlinear viscoelastic response to shear flow. As a consequence of the above shifting procedure, the curves of the steady shear viscosity, the steady shear stress, the first normal stress difference in Fig.4 could be superimposed as shown in Fig.5.

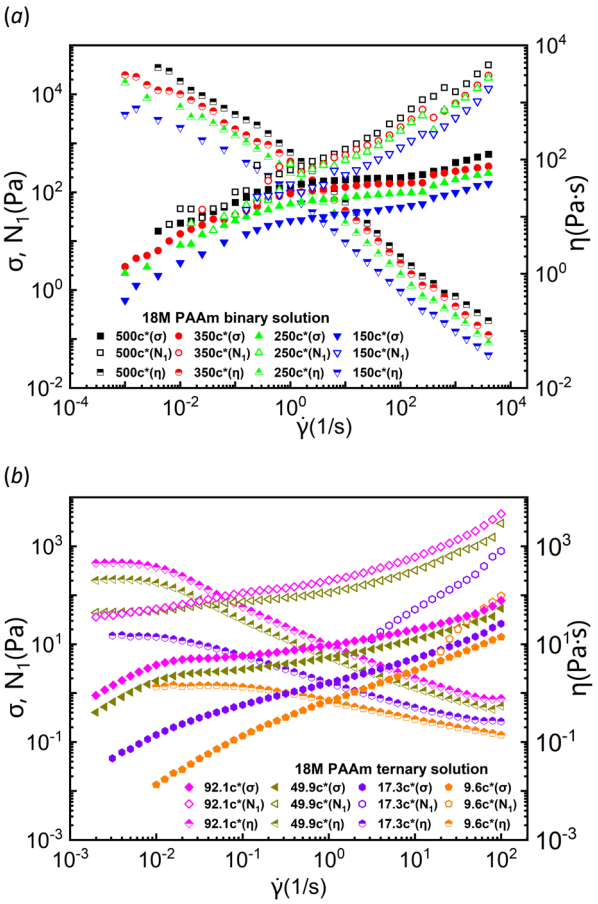

Fig.4 The steady shear stress (σ), the shear viscosity (η) and the first normal stress difference (N_1) are plotted as a function of shear rates for (*a*) 18M PAAm binary solutions and (*b*) 18M PAAm ternary solutions.

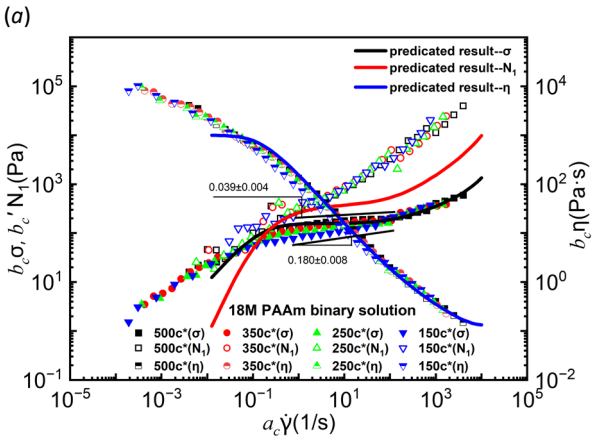

(*b*)

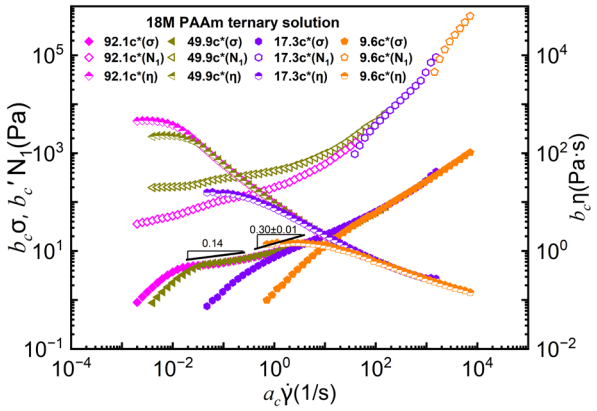

Fig.5 The master curves of the steady shear stress (σ), the shear viscosity (η) and the first normal stress difference (N_1) for (*a*) 18M PAAm binary solutions and (*b*) 18M PAAm ternary solutions.

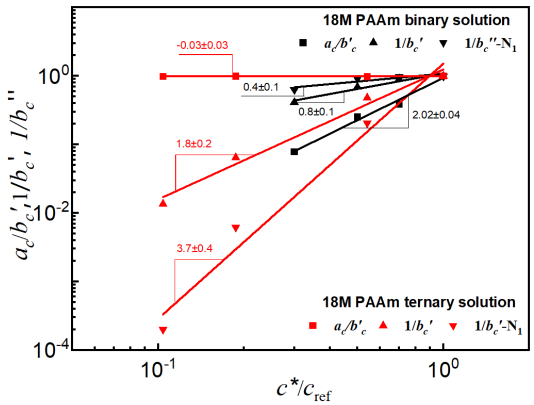

Fig.6 The concentration scaling of the shifting factor a_c/b_c to obtain the master curves of the steady shear viscosity and the first normal stress difference in Fig.5 for the semi-dilute entangled 18M PAAm binary (c_{ref}=500c*) and ternary (c_{ref}=92.1c*) solutions.

Fig.6 shows a power law concentration scaling of the shifting factors (a_c/b_c' , b_c' and $1/b_c''$) for the superposition of the steady shear viscosity, the shear stress and the first normal stress difference, respectively. In comparison with the linear rheometric properties of the same solutions, the concentration scaling exponent of the steady shear viscosity for the 18M PAAm binary solutions significantly decreases to 2.02±0.04. Whereas there is little change for the 18M PAAm ternary solutions. The scaling of its steady shear viscosity is approximately independent of polymer concentration. The results indicate that the Cox-Merz rule holds approximately in the relatively low polymer concentration region.[40] For the binary solution, the scaling exponent of the shear stress, 0.8±0.1, is about double that of its first normal stress difference, 0.4±0.1. Whereas for the ternary solutions, the scaling exponent of the shear stress, 1.8±0.2, is about half that of its first normal stress difference, 3.7±0.4. The 18M PAAm ternary solution shows much stronger concentration scaling than that of the binary solutions. The phenomenon of "shear thinning" is common in semi-dilute entangled 18M PAAm solution with strong elasticity. The slope of the steady-state shear stress in the intermediate shear rate range decreases with the increase of polymer concentration. Noticeably the steady-state shear stress of 500c* 18M PAAm shows a weak dependence on the shear rate with a slope of 0.039±0.004 over the shear rate between 0.5 s^{-1} and 100 s^{-1}. It potentially may cause "transient shear banding" and will be verified qualitatively by a computational study below.

C. Simulation results

For simplicity and without lose much generality in studying transient shear banding, the steady shear rheometric data of 18M PAAm binary solution in Fig.5(*a*) was fitted by the single mode Rolie-Poly model. The results are listed in Table 1, which give a good fit to the steady shear stress and viscosity over a wide range of shear rate from 0.05 s^{-1} and 5000 s^{-1} as shown in Fig.5(*a*). However, the calculated first normal stress difference significantly deviates from the experimental data as shear rate exceeds about 3 s^{-1}. The Rolie-Poly model were solved under simple shear flow in a 200×100×100 or 200×200×1 computational grid and various nominal shear rates. The numerical results were analyzed by Paraview software and reported below.

Table 1 Parameter selection for the single-mode Rolie-Poly model.

mode l	Rolie-Poly
ρ	1000 kg/m^3
η_s	0.001 Pa·s
η_p	1000 Pa·s
λ_D	4 s
λ_R	0.005 s
χ_{max}	3
β	1
δ	-0.5

The shear stress is nearly flat over the nominal shear rate range between 5 s^{-1} and 100 s^{-1}. The simulation results are shown in Fig.7.

Moreover, the shear rate $\dot{\gamma}$=5 s^{-1} is in the middle of the shear stress approximation platform region located in Figure 6. Figure 7(a) shows the distribution of the velocity U_x of the fluid in the y-direction. As can be seen from the figure, the fluid can be divided into two shear bands at 5 s, and the strain rate of the upper one is 33.86 s^{-1}, while the lower one is 0.87 s^{-1}, which can basically correspond to the upper and lower bounds of the steady-state shear stress platform using the Rolie-Poly model, which is also a general feature of the shear band behavior. However, as

the time further increases, the shear band at the upper edge gradually spreads downward by the flow field of the

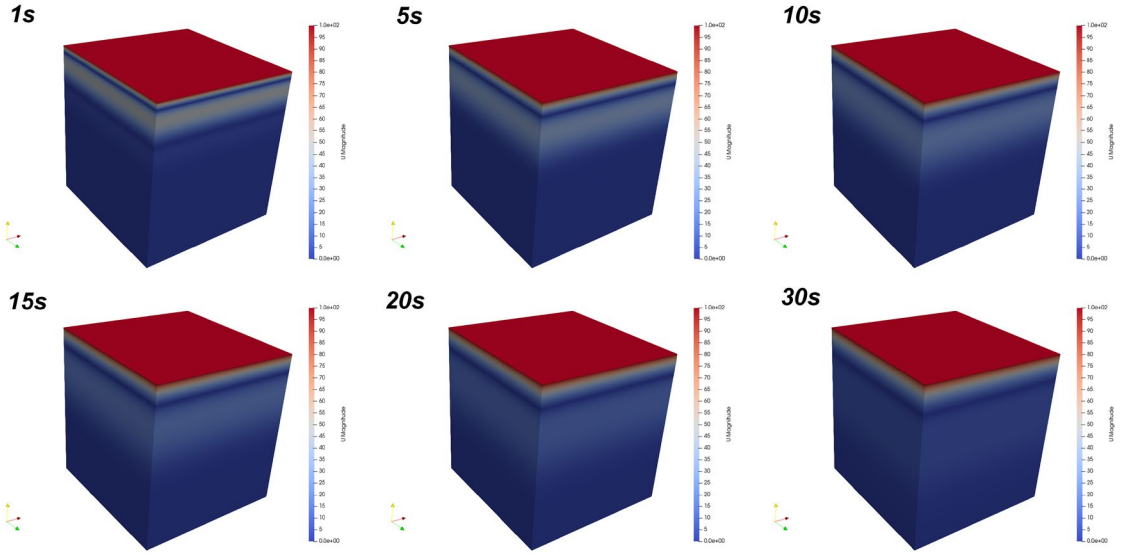

Fig.7 The cloud map of the velocity field along the x-direction from 1s to 30s with the average shear rate $\dot{\gamma}$=100 s^{-1} in three-dimensional simple shear flow.

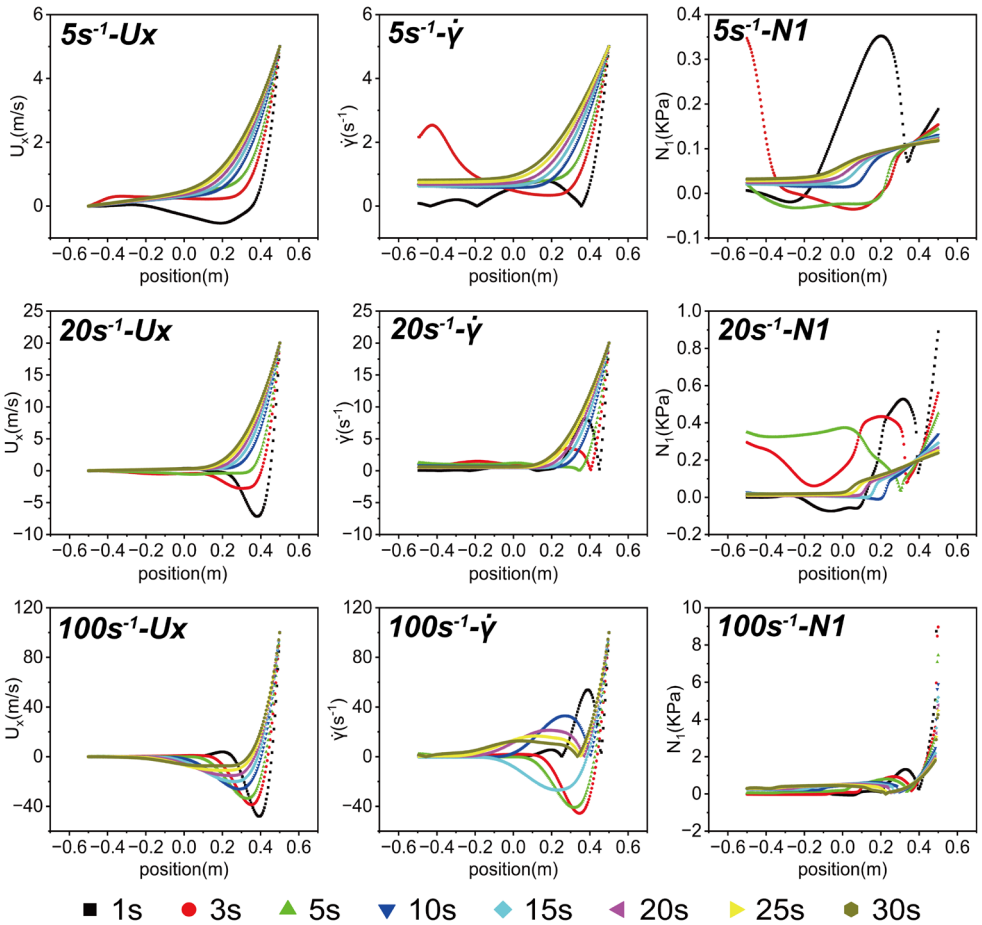

Fig.8 The cloud map of the velocity field along the x-direction from 1s to 30s with the average shear rate $\dot{\gamma}$=100 s^{-1} in three-dimensional simple shear flow.

action, and the thickness of the shear band thus increases. When the simulation time comes to 1000 s, the thickness of the shear band basically increases to the thickness of the whole fluid grid, and the strain rate applied by the whole fluid is 5 s^{-1}. Figure 7(b), 7(c), 7(d) shows the distribution diagram of the first normal stress difference N_1, shear stress τ_{total}, and strain rate $\dot{\gamma}$ during the fluid shear process, respectively. Fig. 7(e) is the average first normal stress difference and the average total shear stress of the entire computing grid (40,000 solutions) change with the simulation time goes, in the early stage of the simulation, they have a larger fluctuations and finally the steady state is reached.

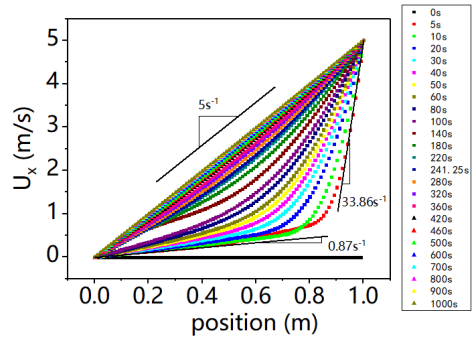

(a)

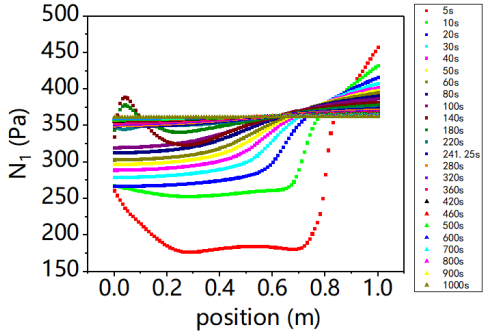

(b)

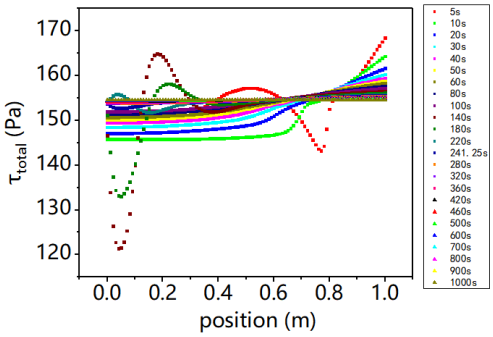

(c)

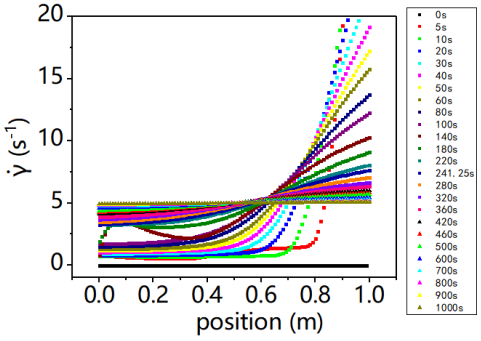

(d)

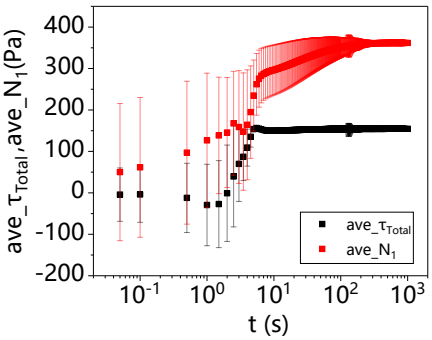

(e)

Fig. 7 Streamline diagram distribution and temporal evolution of multi-physics with an average strain rate of 5 s^{-1} in 2 dimensional simple shear flow.

Also, the velocity distribution U_x of the simulation results at 0.1 s^{-1}, 1 s^{-1}, 20 s^{-1}, 60 s^{-1}, 100 s^{-1} are shown in Figure 8. As shown in the figure 8(a) at 0.1 s^{-1}, the velocity distribution transition from extreme disorder to mild perturbation over 0 s to 10 s, and at 30 s, U_x began to linear increase, further increase the simulation time, U_x still remains unchanged. During this period, U_x did not show significant stratification, that is, no shear bands at the strain rate of 0.1 s^{-1}, consistent with the results shown in Figure 6 that the shear rate of 0.1 s^{-1} was not in the stress platform (stress with a smaller slope), and demonstrated the idea that the entangled polymer solution does not have shear bands below the critical W_i number. Figure 8(b)~(e) shows the applied strain rates of 1 s^{-1}, 20 s^{-1}, 60 s^{-1}, 100 s^{-1}, respectively. The results show the presence of transient shear bands, and the upper shear bands will gradually spread down and eventually disappear over the simulation time, consistent with the results in Figure 7.

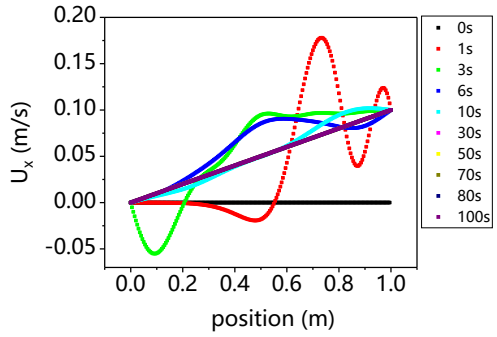

(a) 0.1 s^{-1}

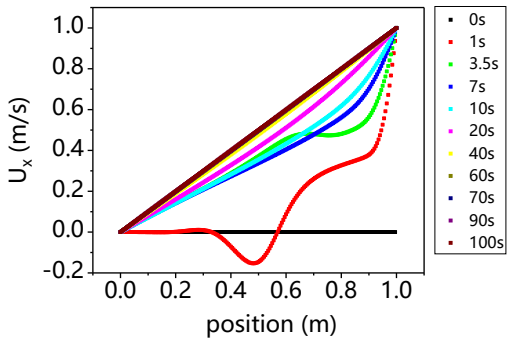

(b) 1 s^{-1}

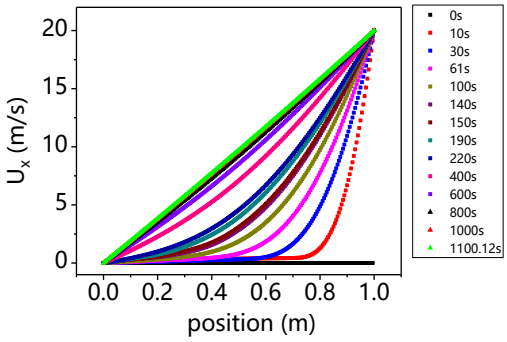

(c) 20 s^{-1}

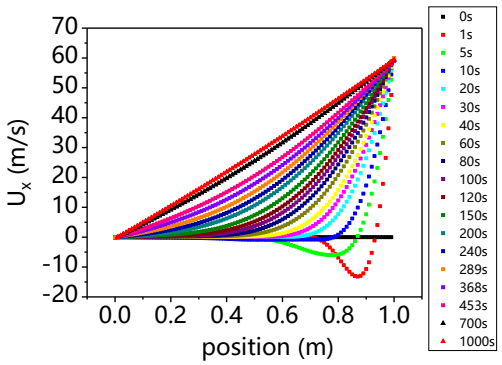

(d) 60 s^{-1}

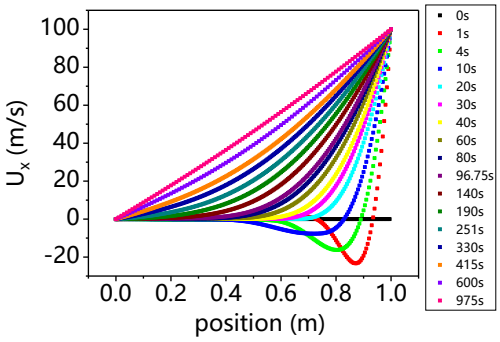

(e) 100 s^{-1}

Fig. 8 The velocity distribution U_x of the simulation results at 0.1 s^{-1}, 1 s^{-1}, 20 s^{-1}, 60 s^{-1}, 100 s^{-1}, corresponding to (a)~(e), respectively.

The above discusses the multi-physics distribution of two-dimensional simple shear flow in the flow field, but the two-dimensional does not reflect the situation in real experiments, for this reason, the following work will discuss the situation of three-dimensional simple shear flow. The choice of model parameters and boundary conditions is consistent with the two-dimensional simple shear flow, with the length of the fluid set to 1 m, the width set to 1 m, and the height set to 1 m. The meshing method is to choose the equally spaced straight line division method, and the grid distribution selected is 100×100×100, that is, each mesh is a cube, and the length of the three directions of x, y, and z is 0.01 m, 0.01 m, respectively.

When the average shear rate is set at 5 s^{-1}, the velocity field at different times (0 s, 410 s, 1020 s) is shown in Figure 9, where (a_1) ~ (a_3) is represented as Ux, (b_1) ~ (b_3) is represented as Uy, and (c_1) ~ (c_3) is represented as Uz. The amplitude of the speed Ux in the x direction is between 0 and 5 m/s, while the velocity amplitude of Uy and Uz is very small, basically within 10^{-7} m/s, that is, Uy = Uz = 0 m / s. At the same time, The position at the centerline were selected as probe positions to study the physics distribution, as shown in Figure 10, where (a) is the comparation of U and Ux ,and (b) is the velocity in the X direction, (c) is the first normal stress difference distribution, (d) is the total shear stress distribution, and (e) is the strain rate distribution. By comparing the U and Ux in figure (a), we find that Uy and Uz do not affect the size of U , so we use the relation of Ux with the position to search the shear banding. Ux also forms a shear banding in the early stages of the simulation, with a high shear rate banding at the top and a low shear rate banding at the bottom. As the simulation time is further extended, the shear banding gradually disappears and the entire flow field becomes a uniform flow field. The corresponding first normal stress difference, total shear stress and shear rate

are initially in a disordered state, and the final flow field becomes a uniform flow field and will remain fixed. The average first normal stress difference and the average total shear stress in the entire flow field have a larger error at the beginning and eventually reach a steady state, as shown in Figure 10 (f).

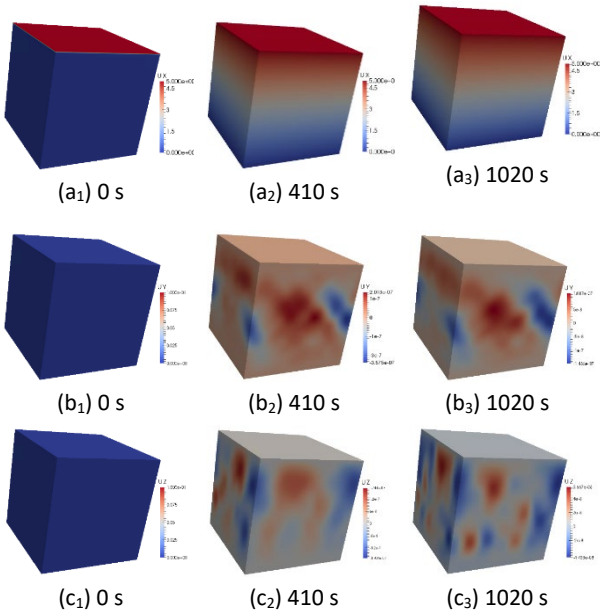

Fig. 9 A cloud map of the velocity field at different moments.

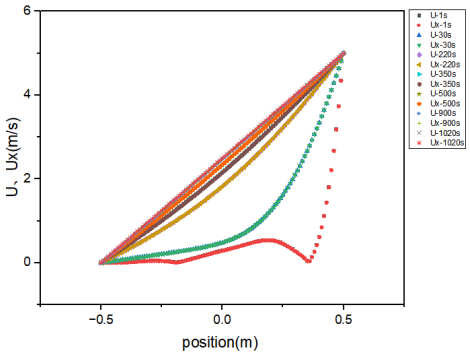

(a)

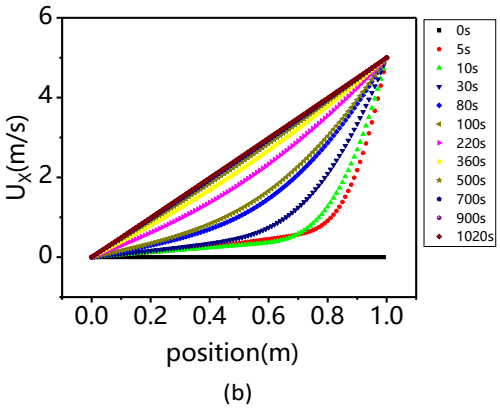

(b)

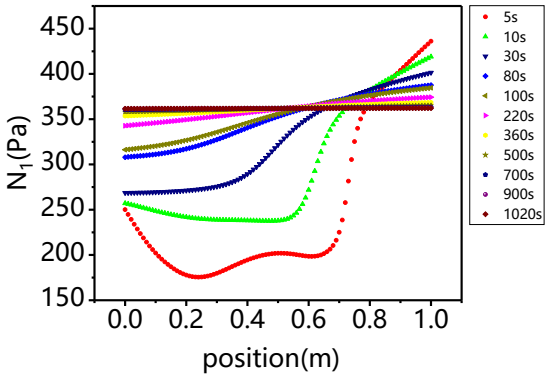

(c)

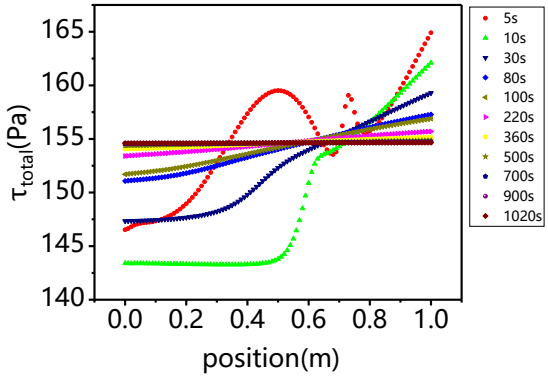

(d)

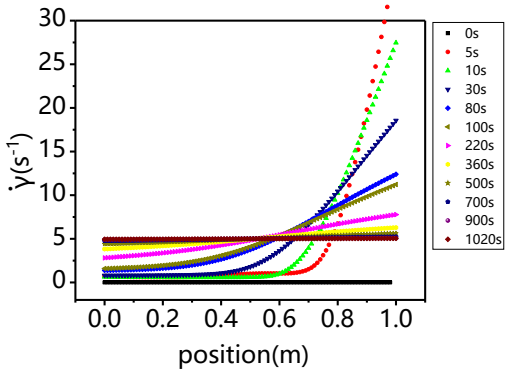

(e)

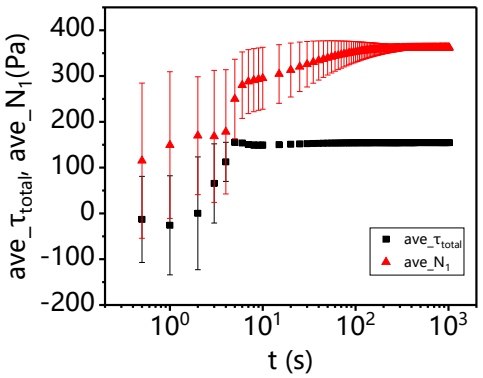

(f)

Fig. 10 Distribution and temporal evolution of multi-physics with an average strain rate of 5 s^{-1} in 3 dimensional simple shear flow.

In conclusion, we can learn from the velocity distribution map that the " transient shear banding" phenomenon of the polymer solution requires a certain shear rate $\dot{\gamma}$, that is, the critical number W_i, in this paper $W_i = \lambda_D * \dot{\gamma}$, where λ_D= 4 s, $\dot{\gamma}$ is for the applied strain rate. When the slope of the shear stress platform region was small positive values, no shear banding was present in 18M PAAm aqueous solution while W_i < 4, and at 4 ≤ W_i < 400, transient shear banding were present in the 18M PAAm aqueous solution. Figure 11 shows the plot of the normalized velocity U_x/U_0 distribution at the absolute simulation time of 80 s for 1 s^{-1}, 5 s^{-1}, 20 s^{-1}, 60 s^{-1}, 100 s^{-1} in 2 or 3 dimensional simple shear flow.It can be found from the figure that at W_i= 4, the flow field has become a uniform flow field, with the larger the $W_i$number, the flow field is the more unstable, the greater the degree of the flow-induced phase separation appears. To more precisely express the time size of the presence of the shear banding, we extracted θ from the normalized velocity U_x/U_0 distribution of these five examples, and θ is defined as the angle of a velocity tangent to a vertical line near the top position, as shown in Figure 11. Figure 12 shows a function of θ/45° and t/λ_D, and at θ = 45°, the flow field appears as a uniform flow field. It shows that as the W_i number increases, the longer the shear banding exists, and the longer the flow field changes from a uniform flow field.

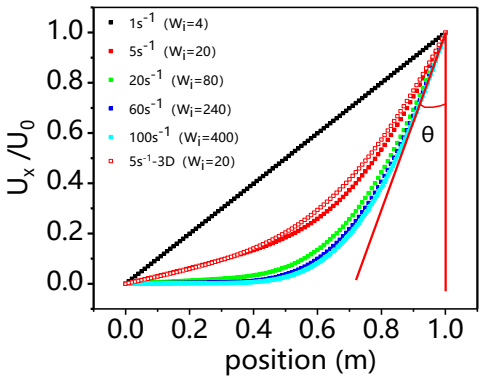

Fig. 11 Normalized velocity U_x/U_0 distribution plot at the absolute simulation time of 80 s for the 1 s^{-1}, 5 s^{-1}, 20 s^{-1}, 60 s^{-1}, 100 s^{-1}.

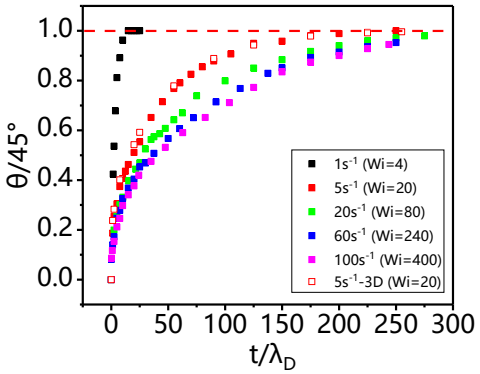

Fig. 12 A function of θ/45° and t/λ_D.

IV. CONCLUSIONS

Here we systematically characterized the universality characteristics of shear banding behavior in 18M PAAm aqueous solutions of 48c* ~500c* from both rheological experiments and computational simulations. The rheological experiments demonstrate that the shear stress does not change with the applied shear rate. At the same time, based on the steady-state flow experiment of rheology, explore the shear banding behavior under a not standard shear stress platform (with a small slope). We used a single-mode Rolie-Poly model to numerically simulate shear banding features and found the emergence of transient shear banding that spread with the simulation time and eventually disappear. Moreover, the transient shear banding depends on the critical W_i number, and as the W_i number increases, the longer the transient shear band exists, the longer the time it takes for the transition to a uniform flow field.

ACKNOWLEDGMENTS

Financial support was provided by the Ministry of Science and Technology of the People's Republic of China under the research grant 2020AAA0104804.

References

1 H. Rehage and H. Hoffmann, *Molecular Physics*, 1991, **74**(5), 933-973.

2 T. Divoux, M. A. Fardin, S. Manneville and S. Lerouge, *Annu. Rev. Fluid Mech.*, 2016, **48**, 81-103.

3 R. Makhloufi, J. P. Decruppe, A. Ait-Ali and R. Cressely, *Europhys. Lett.*, 1995, **32**, 253-258.

4 J. Y. Lee, G. G. Fuller, N. E. Hudson and X.-F. Yuan, *J. Rheol.*, 2005, **49**, 537-550.

5 R. W. Mair and P. T. Callaghan, *Europhys. Lett.*, 1996, **36**, 719-724.

6 M.M. Britton and P. T. Callaghan, *J. Rheol.*, 1997, **41**, 1365-1386.

7 S. Ravindranath and S.-Q. Wang, *J. Rheol.*, 2008, **52**, 341-358.

8 S. Jaradat, M. Harvey and T.A. Waigh, *Soft Matter*, 2012, **8**, 11677-11686.

9 M. E. Cates, *J. Phys. Chem.*, 1990, **94**, 371-375.

10 N. A. Spenley, M. E. Cates and T. C. B. McLeish, *Phys. Rev. Lett.*, 1993, **71**, 939-942.

11 M. Doi and S. F. Edwards, *The Theory of Polymer Dynamics*, Oxford University Press, Oxford, UK, 1986.

12 P. Espanol, X.-F. Yuan, and R. C. Ball, *J. Non-Newtonian Fluid Mech.*, 1996, **65**, 93-109.

13 X.-F. Yuan, *Europhys. Lett.*, 1999, **46**, 542-548.

14 X.-F. Yuan, *Phys. Chem. Chem. Phys.*, 1999, **1**, 2177-2182.

15 O. Radulescu and P. D. Olmsted, *J. Non-Newtonian Fluid Mech.*, 2000, **91**, 143-164.

16 K. Sato, X.-F. Yuan and T. Kawakatsu, *Eur. Phys. J. E*, 2010, **31**, 135-144.

17 M. Doi and A. Onuki, *J. Phys. II*, 1992, **2**, 1631-1656.

18 X.-F. Yuan and L. R. Jupp, *Europhys. Lett.*, 2002, **60**, 691-697.

19 L. R. Jupp, T. Kawakatsu and X.-F. Yuan, *J. Chem. Phys.*, 2003, **119**, 6361.

20 S.M. Fielding and P. D. Olmsted, *Eur. Phys. J. E*, 2003, **11**, 65-83.

21 L.R. Jupp and X.-F. Yuan, *J. Non-Newtonian Fluid Mech.*, 2004, **124**, 93-101.

22 M. Cromer, M. C. Villet, G. H. Fredrickson and L. G. Leal, *Phys. Fluids*, 2013, **25**, 051703-051709.

23 X-W. Guo, S. Zou, X. Yang, X.-F. Yuan and M. Wang, *RSC Adv.*, 2014, **4**, 61167-61177.

24 G. Marrucci, *J. Non-Newtonian Fluid Mech.*, 1996, **62**, 279-289.

25 A. E. Likhtman, S. T. Milner, and T. C. B. McLeish, *Phys. Rev. Lett.*, 2000, **85**, 4550-4553.

26 N. Germann, *Current Opinion in Colloid & Interface Science*, 2019, **39**, 1-10.

27 J. Cao and A. E. Likhtman, *Phys. Rev. Lett.*, 2012, **108**, 028302-028306.

28 S.-Q. Wang, S. Ravindranath, P. Boukany, M. Olechnowicz, R. P. Quirk, A. Halasa and J. Mays, *Phys. Rev. Lett.*, 2006, **97**, 187801-18704.

29 P. Tapadia, S. Ravindranath and S.-Q. Wang, *Phys. Rev. Lett.*, 2006, **96**, 196001-196004.

30 M. Mohaghenhi and B. Khomami, *J. Rheol.*, 2016, **60**, 849-859.

31 M. Mohaghenhi and B. Khomami, *J. Rheol.*, 2016, **60**, 861-872.

32 M. Boudaghi-Khajehnobar, B. J. Edwards and B. Khomami, *Soft Matter*, 2020, **16**, 6468-6483.

33 J. Francois, T. Schwartz and G. Weill, *Macromolecules*, 1980, **13**, 564-570.

34 A. Lanzaro, X-F. Yuan, *J. Non-Newtonian Fluid Mech.* 2011, **166**, 1064-1075.

35 A. E. Likhtman and R. S. Graham, *J. Non-Newton. Fluid Mesh.*, 2003, **114**, 1-12.

36 R. S. Graham, A. E. Likhtman, T. C. McLeish, S. T. Milner, *Journal of Rheology, 2003,* **47**, 1171–1200.

37 K. K. Kabanemi and J.-F. Hétu, *Journal of Non-Newtonian Fluid Mechanics*, 2009, **160**, 113-121.

38 OpenFOAM programmer's guide, OpenFOAM programmer's guide (Version 2.1.0), 2013.

39 F. Pimenta and M.A. Alves, RheoTool User Guide (Version 5.0), https://github.com/fppimenta/rheoTool, 2020.

40 Y-Q. Fan, A. Lanzaro, X-F. Yuan, *Chinese Journal of Polymer Science*, 2022, https://doi.org/10.1007/s10118-022-2757-6.